Percolation versus depinning transition : The inherent role of damage hardening during quasi-brittle failure

Ashwij Mayya

Percolation versus depinning transition : The inherent role of damage hardening during quasi-brittle failure

Ashwij Mayya*
Institut Jean Le Rond D'Alembert UMR 7190, Sorbonne Université, CNRS, Paris, France
(Dated: October 22, 2023)

The intermittent damage evolution preceding the failure of heterogeneous brittle solids is well-described by scaling laws. In deciphering their origins, failure is routinely interpreted as a critical transition. However, at odds with expectations of universality, a large scatter in the value of the scaling exponents is reported during acoustic emission experiments. Here we numerically examine the precursory damage activity to reconcile the experimental observations with critical phenomena framework. Along with disorder, we consider an additional parameter that describes the progressive damageability of material elements at mesoscopic scale. This hardening behavior encapsulates the micro-fracturing processes taking place at lower length scales. We find that damage hardening can not only delay the final failure, but also affect the precursory damage activity. For large hardening, the long-range elastic interactions prevail over disorder, ensuring a nearly homogeneous damage evolution before failure that takes place through damage localization, a standard instability. Damage bursts observed prior localization are then reminiscent of depinning transition. On the contrary, when hardening is low, precursors that are still described by scaling laws, are a signature of percolation. The existence of two classes is highlighted by the different values of the exponent characterizing the divergence of the precursor size on approaching failure. Our findings shed new light on the connection between the level of quasi-brittleness of materials and the statistical features of the failure precursors. Finally, they provide a more complete description of the acoustic precursors and thus pave the way for quantitative techniques of damage monitoring of structures-in-service.

I. INTRODUCTION

Failure of heterogeneous solids takes place through intermittent bursts of localized damage activity [1–3]. The acoustic emissions accompanying the precursory activity are scale-invariant. The source-map of such events reveals a progressively coherent spatial and temporal distribution of events that finally localize along a plane at failure [4, 5]. They assert the collective nature of damage growth in heterogeneous solids. And yet, apart from the presence of power laws, a comprehensive understanding of the precursory damage accumulation remains elusive. Consequently, its connection with failure itself, is also not clear.

The scale-free statistics of precursors strongly argues for an interpretation of failure as a critical phenomenon [6–14]. Indeed, both energy and frequency of acoustic hits are shown to increase on approaching failure. However, a careful examination of the experimental data reveals that such an interpretation may not straightforward [15]. In particular, the exponent $\alpha_{N_{\rm AE}}$ describing the increase, $dN_{\rm AE}/dt \sim |t_{\rm c} - t|^{-\alpha_{N_{\rm AE}}}$ of the activity rate $dN_{\rm AE}/dt$ close to failure at time $t_{\rm c}$ displays a wide-range of values. During compressive failure, values ranging from 0.5 upto 0.75 are reported in case of synthetic SiO_2 and rocks [10, 16–18], concrete [14], and $\alpha_{N_{\rm AE}} \simeq 1.0$ is reported for complex materials such as shale [16] and teeth [19]. For tensile failure, the value of $\alpha_{N_{\rm AE}}$ is even higher : 1.4 for un-notched specimens of paper during uniaxial tension tests [11], 1.68 and 1.28 for specimens of bamboo chopsticks [20] and marble [21], respectively during three-point bending tests [22]. Such a scatter is at odds with the expectations of an universal exponent, a hall-mark of critical phenomena. Even the exponent $\tau_{\rm AE}$ characterizing the distribution of the energies of the acoustic emissions, $P(E_{\rm AE}) \sim E_{\rm AE}^{-\tau_{\rm AE}}$ is found to vary from 1.3 upto 1.8 in experiments involving different brittle solids [6–11, 14–20, 23].

Independent of the experiments, numerical studies of fracture focus on the interplay between disorder and elastic interactions. These phenomenological models often consider an assembly of brittle elements with distributed thresholds. Damage evolution corresponds to a series of correlated breakage events [24–35]. As a result, except for weak disorder, failure is accompanied by scale-invariant precursors [30, 31]. Surprisingly, these observations have been interpreted as a signature of either discontinuous (first-order) or continuous (second-order) transitions. In the first case, the seemingly critical aspects of precursors were attributed to the sweeping of an instability [26–28, 32, 36]. Whereas in the second case, percolation of damage clusters was proposed [24, 29, 31, 34]. In addition to disorder, the functional form of the elastic interactions is also shown to affect the results of these numerical models [34, 37–39]. Overall, rationalizing these numerical observations in relation to the experiments is also rather difficult.

To reconcile the various contrasting interpretations, we recently proposed a damage mechanics based framework for compressive failure of disordered solids [40, 41]. It revealed the subtle connection between the intermittent dynamics of damage evolution and the out-of-equilibrium physics of disordered systems. Using a combined exper-

* ashwij@dalembert.upmc.fr

imental and theoretical approach, we showed the precursory damage activity to be reminiscent of the depinning dynamics of a non-standard driven elastic interface [42, 43]. At the same time, the evolution toward failure was described by the non-stationary evolution of the interface culminating in a loss of stability. As a result, the salient features of the precursory activity namely, the size, the spatial extent and the duration were described by critical exponents, reminiscent of depinning transition. Whereas, the power law divergence on approaching failure was a signature of a standard bifurcation in the damage evolution. Interestingly, a combination of these two phenomena provided numerous time-to-failure scaling laws that are useful for predicting failure from precursors [44]. A subtle but important aspect of our framework [40, 41] was the consideration of damage hardening at the local scale. Large hardening leads to a ductile response of the meso-scale elements. This behavior is in good agreement with various experimental observations, especially during compressive failure [45–51]. On the contrary, traction tests often present a short damage accumulation phase or even abrupt failure at the mesoscopic length scale. While these different behaviors can be captured by considering different hardening laws, the connection between the ability of a material to progressively damage (harden) before failure and the statistics of precursors is not clear. However, this understanding may be relevant in engineering applications particularly for the anticipation of failure from precursor statistics.

Here we examine the failure of heterogeneous solids using a numerical model that explicitly accounts for the cooperativity between disorder and elastic interactions during the intermittent damage evolution [13, 52–54]. One of our main findings is the observation of a brittle-to-ductile transition as hardening is increased beyond a threshold value. The precursory activity is also different in both regimes : We show that they belong to two different critical phenomena frameworks. When hardening is low, the intermittent damage evolution is dominated by the disorder. Material failure is then reminiscent of percolation [24, 29–31]. However, when hardening is large, precursors resemble avalanches observed in driven disordered elastic interfaces, and is thus reminiscent of a depinning transition [40, 41]. Strikingly, the nature of the failure point is also then altered. Contrary to the critical point description for failure during percolation, when hardening is large, failure corresponds to the onset of damage localization, a standard instability. This difference is highlighted in the approach to failure. The exponent characterizing the power law divergence of precursors on approaching the percolation threshold is larger than the value measured for instability. Our findings provide new insights on the connection between the level of quasi-brittleness and the precursor statistics. They also provide a possible explanation for the scatter in the scaling exponents observed in acoustic emission experiments.

II. MODEL DESCRIPTION

We first briefly present the theoretical framework for the intermittent damage evolution that precedes the failure of brittle disordered specimens [40, 41, 54]. It derives from damage mechanics which provides a mesoscopic scale description of the dissipative processes at lower length scales as a gradual increase in local damage level $d(\vec{x},t)$ at the location $\vec{x}$ and time t. The increase of the average damage level $d_\circ$ drives the degradation of the macroscopic scale stiffness $E_\circ$ [55]. The applied stress $\sigma_{\rm ext}(t)$ imposed by the test machine, along with the boundary conditions (e.g., confinement) provides the state of stress at the specimen scale $\sigma_\circ(t)$. To deduce the damage growth at the material element $(\vec{x},t)$, we use an energy criterion similar to the one used in fracture mechanics. We compare (i) a loading dependent local driving force $Y[d(\vec{x},t),\sigma_\circ]$ which provides the rate of elastic energy released for an incremental growth of damage with (ii) the local damage resistance $Y_{\rm c}[d(\vec{x},t)]$, the threshold value corresponding to the rate of energy dissipated for an incremental growth of damage [53, 54]. The damage criterion then writes as

$$\begin{aligned} &Y[d(\vec{x},t),\sigma_\circ] < Y_{\rm c}[d(\vec{x},t)] \rightarrow \text{stable damage,}\\ &Y[d(\vec{x},t),\sigma_\circ] = Y_{\rm c}[d(\vec{x},t)] \rightarrow \text{damage grows.}\end{aligned} \tag{1}$$

To track the damage evolution at small timescales, we consider an initial reference damage level $d_\circ(0)$ at which the driving force and the damage resistance are $Y_\circ[d_\circ,\sigma_\circ]$ and $Y_{\rm c\circ}(d_\circ)$, respectively. We then focus on the evolution of the perturbations that follow as $\Delta\dot{d}(\vec{x},t) \propto \Delta Y[\Delta d(\vec{x},t),\sigma_\circ] - \Delta Y_{\rm c}[\Delta d(\vec{x},t)]$, assuming an over-damped dynamics. The right hand side of this relation describing the generalized driving force for damage growth can be organized in three terms as

$$\begin{aligned}\Delta\dot{d}(\vec{x},t) \propto &\mathcal{K}(\sigma_\circ)\left[v_{\rm m}(\sigma_\circ)\,t - \Delta d(\vec{x},t)\right] + \\ &\psi(\sigma_\circ) * \left[\Delta d(\vec{x},t) - \langle\Delta d\rangle_{\vec{\rm x}}\right] - y_{\rm c}[\vec{x},d(\vec{x},t)].\end{aligned} \tag{2}$$

Here $\mathcal{K}(\sigma_\circ) = \frac{\partial(Y_{\rm c\circ}-Y_\circ)}{\partial d_\circ}$ controls the stability of damage evolution and $v_{\rm m}(\sigma_\circ)$ provides the dissipation rate during damage spreading. On approaching failure $\mathcal{K}$ approaches zero and $v_{\rm m}$ diverges as a power law. The second (non-local) term of Eq.(2) describes the long-range interactions in the damage field taking values based on the perturbations in the damage field$\Delta d(\vec{x},t)$. For the current case of failure during uniaxial loading along the vertical axis, we derive the interaction kernel using the method described in Dansereau *et al.* [53] as

$$\psi(\sigma_\circ) = \left[\frac{E'(d_\circ)^2}{E(d_\circ)^3}\right](1-\nu^2)\sigma_{\rm ext}^2\left[\frac{x^4-3y^4+6x^2y^2}{4\pi(x^2+y^2)^3}\right]. \tag{3}$$

In practice, the kernel $\psi(\sigma_\circ)$ describes the driving force redistribution in $\vec{x} \neq \vec{x}_0$ following an incremental damage growth at $\vec{x} = \vec{x}_0$. We find $\psi(\sigma_\circ) \sim 1/r^2$ where r is

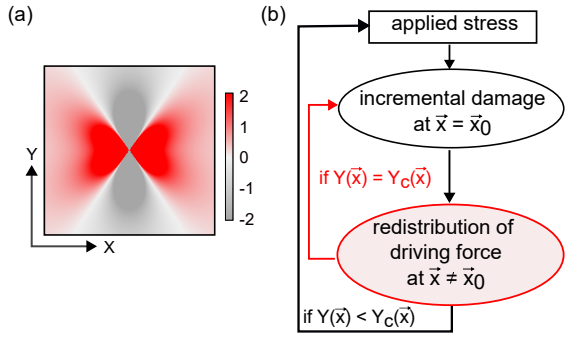

FIG. 1. (a) Functional form of the kernel $\psi(\sigma_\circ)$ for the case of uniaxial compression in 2D. (b) Schematic of the feedback-loop during the intermittent damage evolution in disordered solids.

the radial distance from the damaged element. The functional form of the kernel is shown in Fig. 1(a). We note its quadru-polar symmetry that imposes only a particular region of the specimen is reloaded after an elementary damage event, here along directions perpendicular to the loading axis. The last term $y_c[\vec{x}, d(\vec{x}, t)]$ in the evolution equation (2) describes the material disorder. The detailed explanation of our approach including the derivation of the interaction kernel $\psi(\sigma_\circ)$ is provided in Mayya *et al.* [41]. We note the resemblance of Eq. (2) to the equation of motion of driven disordered elastic interfaces [42, 43]. This readily allows for an interpretation of the intermittent damage evolution as avalanches during the depinning of a elastic interface (representative of the damage level) driven over a disordered field of damage resistance. It also provides insights on the stability of the damage evolution process during the approach to failure [40, 41].

Damage hardening

From Eq. (2), we see that ensuring stable damage growth $\mathcal{K} > 0$ requires the value of damage resistance to increase with damage level. Following the damage criterion, we consider a linear hardening $Y_{c\circ}(d_\circ) = Y_c^\circ(1 + \eta d_\circ)$ where Y_c° is the characteristic damage resistance and η is the hardening coefficient. As a result, the first term of the stability criterion $\mathcal{K}(\sigma_\circ) = \frac{\partial(Y_{c\circ} - Y_\circ)}{\partial d_\circ}$ that derives from the hardening writes as

$$\frac{\partial Y_{c\circ}}{\partial d_\circ} = Y_c^\circ \, \eta. \tag{4}$$

To study the effect of damage hardening, we will consider a constant Y_c° and vary the hardening coefficient η in the following.

Hardening behavior can be therefore directly attributed to the mesoscopic scale description adopted here. Damage evolution at the local level corresponds to expending the distribution of micro-fracturing thresholds, starting from the lowest values. Such a multi-scale interpretation may bridge the discrete failure models such as (global load sharing) fiber-bundle to the damage mechanics framework that considers materials as homogeneous continua [56]. In effect, damage hardening ensures the progressive degradation of stiffness at mesoscopic scale, an observation consistent with the experimental observations [45–51]. Stiffness degradation with increasing damage is extensively discussed in literature [12, 35, 47, 49, 57–60]. Importantly, we obtain a prolonged damage accumulation phase prior to peak load, a failure behavior that is relevant for the safe design of structures.

Numerical implementation

We numerically solve the evolution equation (2) following the protocol presented in Fig. 1(b). We increase the stress such that the damage criterion is satisfied at only one of the material elements $\vec{x} = \vec{x}_0$. Then imposing the damage growth $d(\vec{x}_0, t) = d(\vec{x}_0, t) + \delta d_\circ$ increases the local driving force $Y[d(\vec{x}_0, t), \sigma_\circ]$ and the local damage resistance $Y_c[d(\vec{x}_0, t)]$ by $\frac{\partial Y_\circ}{\partial d_\circ}\delta d_\circ$ and $\frac{\partial Y_{c\circ}}{\partial d_\circ}\delta d_\circ$, respectively. It stabilizes the damage locally as $\mathcal{K} = \frac{\partial(Y_{c\circ} - Y_\circ)}{\partial d_\circ} > 0$ until failure. The elastic energy redistribution that follows may result in one or more elements undergoing damage. Thus, a cascade of damage events may be set-off which is complete when the redistributions are overcome by disorder. As a result, damage during force control experiments evolves by bursts that are separated by elastic loading.

For the numerical modeling, we consider a grid of size $L = 51$ discretized into L^2 elements with periodic boundary conditions. The redistributions after individual damage events are given by Eq.(3), the interaction kernel $\psi(\sigma_\circ)$ corresponding here to the case of uni-axial loading [41]. The variation of the elastic modulus $E_\circ$ with damage is taken as $E_\circ(d_\circ) = E^\circ(1 - d_\circ)^2$ with $E^\circ = 1.01$MPa. The choice of the polynomial function is motivated by the stability criterion that involves the second derivative $E_\circ''(d_\circ)$, see Appendix C. We consider the initial disorder distribution in the damage resistance as a Gaussian $\mathcal{N}(0, \beta)$. The characteristic damage resistance in the hardening rule is taken as $Y_c^\circ = 1.4$ kJ/m^3. The incremental damage $\delta d_\circ$ is set to 0.005. The hardening $\frac{\partial Y_{c\circ}}{\partial d_\circ}\delta d_\circ = Y_c^\circ \eta \delta d_\circ$ that follows the incremental damage at the elements $\delta d_\circ$ is drawn from a narrow Gaussian distribution with a standard deviation of 0.05. The choice of values for E°, Y_c° and $\delta d_\circ$ is similar to the experimental observations of Mayya *et al.* [41]. However they do

TABLE I. Values of disorder and hardening being investigated in this study.

material disorder, β	: 0.05, 0.1, 0.15, 0.2, 0.25, 0.3, 0.35, 0.4, 0.45, 0.5
hardening coefficient, η	: 0.05, 0.5, 1, 2.0, 2.5, 3, 5, 10, 15, 25

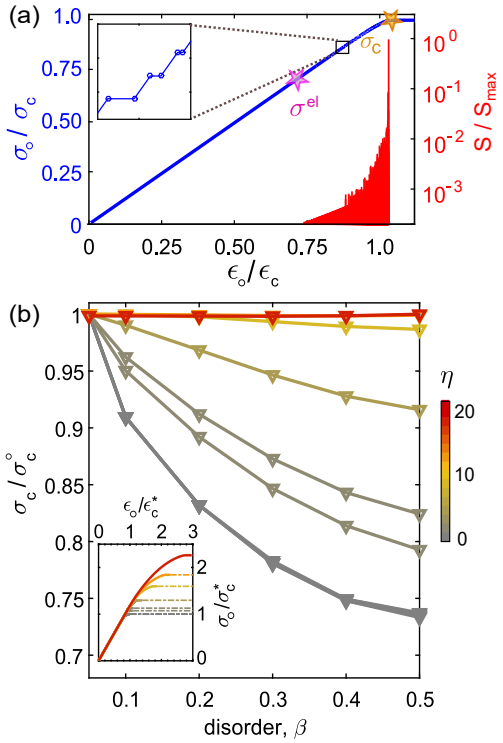

FIG. 2. (a) Typical stress-strain response (in blue) from the damage model obtained for the hardening coefficient $\eta = 2.5$ and disorder $\beta = 0.2$. Inset: Damage cascade manifests at the macroscopic scale as a stress plateau. The size of precursors S normalized by the maximum value $S/S_{\max}$ (in red) is shown to increase on approaching failure. (b) Variation of the normalized critical stress σ_c/σ_c° with the strength of disorder β for different values of the hardening coefficient η. Here σ_c° is the value for the case of disorder $\beta = 0.05$. Inset: Effect of damage hardening on the stress-strain response for a fixed disorder $\beta = 0.2$. σ_c^* and ϵ_c^* are the values of stress and strain at the onset of failure for the case $\eta = 0.05$.

not affect the insights from the study. The range of the disorder β and the hardening coefficient η considered for the present study are given in Table I.

III. RESULTS

The typical stress-strain response (in blue) obtained from the simulations with moderate disorder and low hardening is shown in Fig. 2(a). Beyond the elastic limit $\sigma_{\rm el}$, we find the macroscopic response is a sequence of stress plateaus and elastic loading segments (see inset of Fig. 2(a)). The stress plateaus correspond to dissipative bursts of mechanical energy as shown in Fig. 2(a) (in red). At the local level, a cascade of micro-instabilities in the damage field are progressively stabilized by either disorder or by the unloading during the elastic energy redistributions. However, at the stress σ_c, the damage evolution in force control becomes unstable resulting in a catastrophic failure.

To decipher the role of the damage hardening η, we start by examining the failure stress σ_c. At a fixed disorder strength β, increasing the damage hardening manifests a higher values of critical stress σ_c as well as critical strain ϵ_c, see inset of Fig. 2(b) (also Appendix A). This is consistent with the increased ductility at the local scale. However, when hardening η is fixed, the role of disorder is not straightforward. We find that the specimen strength σ_c decreases with increasing disorder strength β especially when hardening η is small, as shown in Fig. 2(b). For large hardening, however, the strength σ_c is nearly independent of the disorder. Notably, this is at odds with earlier studies that considered brittle constitutive response at the local scale [30–33]. The non-trivial effect raises new questions on the connection between damage hardening and nature of failure. Contrary to the central role of the disorder in the critical point interpretation of failure, here we find that the role of disorder is diminished as hardening is increased. The nature of failure may indeed vary with damage hardening. It then follows that such a transition will also reflect in the scaling description of failure precursors.

A. Criticality during the approach to failure

To decipher the role of damage hardening, we now examine the statistics of precursors. In Fig. 2(a), we find that the precursor size S increases close to failure. To contextualize their evolution, we define the distance to failure $\delta = (\sigma_c - \sigma_\circ)/(\sigma_c - \sigma_{\rm el})$ and measure the variation of the dissipation rate $dE_{\rm d}/dt$ with δ. We note that $dE_{\rm d}/dt \sim \langle S \rangle$, the average size of the precursors [41]. We find the energy dissipation to increase as a power law with the distance to failure $dE_{\rm d}/dt \propto \delta^{-\alpha}$ for nearly all values of disorder and hardening. The value of the exponent α is, however, not a constant.

From the exponent α for different values of disorder and hardening coefficient, we obtain a phase diagram providing the material quasi-brittleness as a function of β and η, see Fig. 3. The bottom left corner of this diagram and its vicinity correspond to weak disorder and low hardening in Fig. 3, and describe brittle failure (in black). Here the precursory activity is scarce and we did not characterize their statistics. Increasing the strength of disorder, we obtain a quasi-brittle failure behavior, an observation that is in good agreement with *toy models* provided in the literature [30–32]. Here, the value of the exponent $\alpha \simeq 0.9$. We now examine the role of damage hardening. In presence of moderate hardening, we obtain a smaller value of exponent α. Notably, even when the disorder is weak, we find $\alpha \simeq 0.5$ (see e.g. $\beta \simeq 0.05, \eta \simeq 5.0$). Similarly when hardening is large, the value of exponent $\alpha \simeq 0.5$. To explain these behaviors, we now analyze in detail, the representative cases of each regime.

In Fig. 3, we consider regimes I and III as typical of the damage spreading when hardening is small and

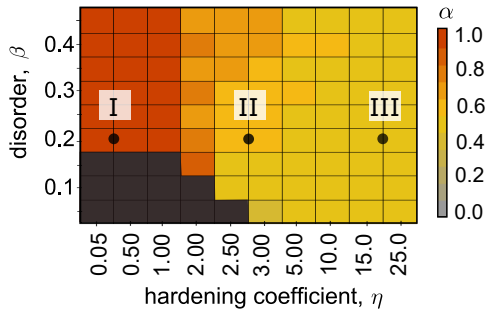

FIG. 3. Values of the exponent α characterizing the power law divergence of dissipation rate on approaching failure for different values of disorder β and hardening coefficient η. We note the bins on the abscissa to be non-uniform.

large, respectively and nominally consider the transition as regime II. We take two sets of data for each regime $\eta = \{0.05, 0.5\}; \{2.5, 3.0\}; \{15, 25\}$ at a fixed disorder strength $\beta = 0.2$. The divergence of the average precursor size $\langle S \rangle$ with the distance to failure δ is shown in Fig. 4(a) for each case. The scaling exponent $\alpha = 0.9 \pm 0.04$ for regime I, $\alpha = 0.55 \pm 0.02$ for zone II and $\alpha = 0.46 \pm 0.01$ for zone III. Beyond different exponents, we find the smallest value of δ reached at failure is different from one regime to another. The rather prolonged precursory phase goes along with a smaller exponent and

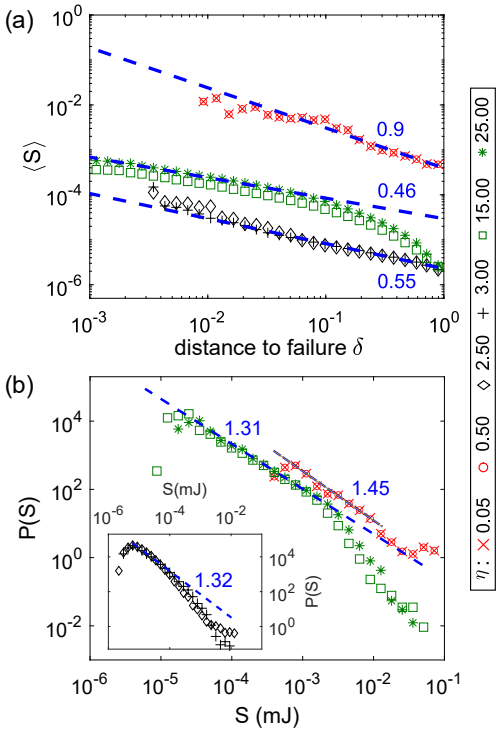

FIG. 4. (a) Divergence of the average precursor size $\langle S \rangle$ with the distance to failure δ. (b) Distribution of the precursor sizes S from data obtained close to failure $\delta \to 0$ for regimes I and III (main panel) and regime II (inset).

highly intermittent damage evolution. Moreover, at a fixed distance to failure, the precursors in regime I are typically larger than the precursors in regimes II and III.

We then compute the distribution of precursor sizes S close to failure ($\delta \to 0$) and obtain a power law $P(S) \propto S^{-\tau}$ for all data-sets as shown in Fig. 4(b). The exponent in regimes II and III was $\tau = 1.31 \pm 0.05$ and $\tau = 1.32 \pm 0.1$, respectively. For precursors from regime I, a higher value $\tau = 1.45 \pm 0.05$ is obtained.

The scale-free statistics of precursors and their divergence as failure is approached seemingly argue for a critical phenomenon interpretation [6–14]. In Mayya *et al.* [41], we untangled these very same features during compressive failure by showing that precursors are avalanches reminiscent of the depinning of a non-standard disordered elastic interface [42, 43]. Failure, on the other hand, was shown to correspond to the onset of localization, a standard instability in the homogeneous damage evolution. The power law divergence of the dissipation rate in this case is then obtained by a linearization of the damage evolution equation (2) providing a theoretical prediction for the exponent $\alpha = 1/2$ [40, 41].

As the values of damage hardening $\eta = \{15, 25\}$ in regime III are comparable to the one measured in the experiments of Mayya *et al.* [41] ($\eta \simeq 45$), we interpret the precursors obtained for large damage hardening as depinning avalanches. Also, the value of $\alpha \simeq 0.46$ matches rather well with the theoretical prediction. In Mayya *et al.* [41], the stress at failure derived using the assumptions of homogeneous damage evolution considerations was nearly independent of the strength of disorder, a prediction that is in rather good agreement with the variations of σ_c with disorder β for regime III, see Fig. 2(b). For the case of moderate hardening, we also find $\alpha \simeq 0.5$ (see Fig. 4(a)). But there is a slight variation in the failure stress with disorder. However, precursors in regime I provide an exponent $\alpha \simeq 0.9$ that is significantly larger.

B. Criticality of precursors for low hardening

To explain the different behavior of precursors in regime I, we examine the elements undergoing incremental damage. As shown in Fig. 5(a), the element selected as the seed, i.e., the first damaged element in a cascade is affected by hardening. We find the damage resistance of the seed Y_c^{seed} to be constantly lower than the average value $Y_c^{\text{seed}} < \langle Y_c \rangle_x$. This is at odds with regime II and III for which beyond a transient stage, the damage resistance of the seeds is comparable to the average value $Y_c^{\text{seed}} \sim \langle Y_c \rangle_x$. This last behavior suggests the participation of all elements during the damage spreading process. It also supports the assumption of homogeneous damage evolution. In contrast, for regime I, only weaker elements of the damage resistance field participate in avalanches, even very close to failure. Clearly, the damage fields of these regimes merit a closer look and will be discussed later in section III C.

We now focus on the incremental damage evolution of the elements. The variation of the average incremental damage Δd^* computed per element during a cascade as a function of the distance to failure, δ is shown in Fig. 5(b). The material elements during regime I, fail completely ($\Delta d^* = 1.0$). As a result, on approaching failure, the concentration of failed elements p increases rapidly close to failure, see inset of Fig. 6(a). In contrast, the material elements for regimes II and III participate only once during damage cascades as $\Delta d^* = \delta d_\circ$, the incremental damage taken to be 0.005 in the present study, as shown in Fig. 6(a). The concentration of failed elements p is therefore (nearly) zero during most of the damage accumulation when damage hardening is (moderately) large.

These disparities in the damage evolution further argue for a different universality class for damage spreading of regime I. In particular, the strong influence of disorder, the participation of weaker elements and an increasing concentration of the failed elements on approaching failure are in violation with the framework describing failure as the depinning of a non-stationary disordered elastic interface [41]. These aspects are rather reminiscent of percolation type damage spreading observed in discrete models [24, 29–32, 37, 61]. In these studies, as driving is increased, numerous clusters of failed elements nucleate and merge with existing ones; Their size increases until failure takes place when a system-spanning cluster ruptures the remaining backbone.

To further examine this idea, we study the distribution of cluster sizes s_c in the damage field prior to failure, see inset of Fig. 6(b). We obtain the scaling relation $P(s_c) \sim s_c^{-\tau_c}$ with $\tau_c = 2.18 \pm 0.1$. This exponent is in rather good agreement with the predicted value 2.05

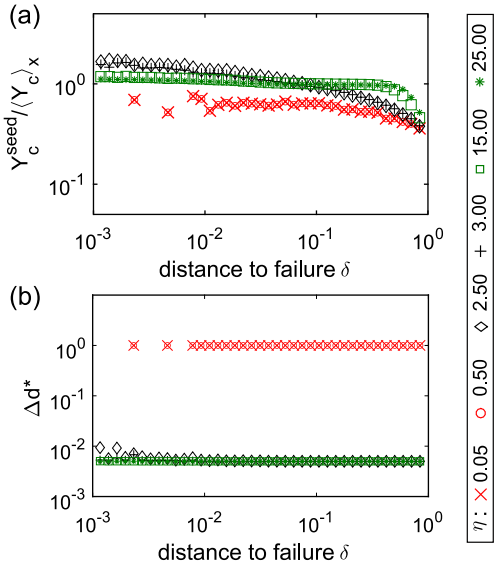

FIG. 5. Variation of (a) the damage resistance of the avalanche seed Y_c^{seed} normalized by the average value $\langle Y_c \rangle_x$ and (b) the average incremental damage Δd^* in the activated elements during the cascade with the distance to failure δ.

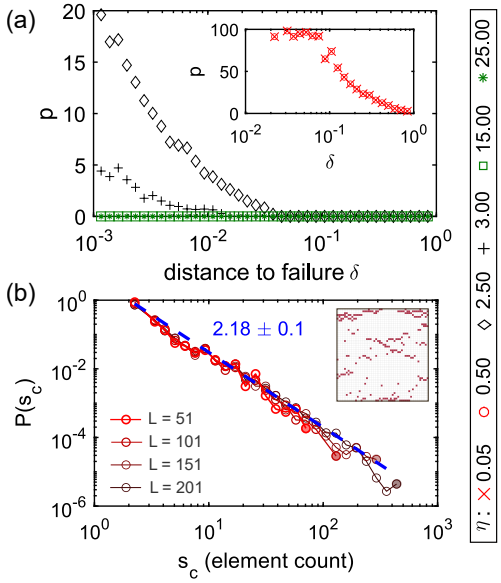

FIG. 6. (a) Variation of the concentration of failed elements p with the distance to failure δ. Inset: Variation of p with δ for regime I. (b) Distribution of the size of the clusters in the damage field when the damage hardening is low ($\eta = 0.5$) and the disorder is moderate ($\beta = 0.2$) for varying specimen size L. The largest clusters in each case are marked as solid circles. Inset: Damage field before failure in a typical specimen of size $L = 51$.

at the percolation threshold in 2D [30]. This scaling is shown to be independent of the specimen size $L \in [101, 151, 201]$. Interestingly, we note in Fig. 6(b), the size of the largest cluster increases with specimen size suggesting finite-size effects. Finally, the exponent $\alpha \simeq 0.9$ in regime I is in rather good agreement with the value $\alpha \simeq 0.86$ reported in case of a 2D fiber bundle model with global load sharing [37, 61]. Strikingly, these results provide a critical point description of failure instead of an instability [40, 41]. Estimating the stress at failure is then not straightforward.

The difference in the nature of failure is also clearly evidenced from the damage field. Contrary to regime III, at the onset of failure, the damage field in regime I is strongly heterogeneous, see top panel of Fig. 7. The Larger the hardening, more homogeneous the damage evolution. Interestingly, all regimes display a thin band within which the damage concentrates at the onset of failure. Outside this band, the damage field contains the signature of the precursors. On the one hand, in regime I, we observe numerous clusters that are nearly linear highlighting the role of the interaction kernel $\psi(\sigma_\circ)$ that prescribes reloading of the driving force along the horizontal axis. For regime II, we find a similar damage field. However, the damage level in the elements for this case is rather distributed. On the contrary, the damage field outside the localization band in regime III appears to be nearly homogeneous. As the strength of disorder at the beginning of the damage accumulation in all three

cases was fixed ($\beta = 0.2$), these observations argue for a connection between hardening and elastic interactions.

C. Effect on the damage feedback-loop

We now interpret the effect of hardening through the competition between disorder and elastic interactions [34, 39]. Using the original distribution $P(y_c)$ in the damage resistance as reference (black curve), we track the events during a typical damage cascade as shown in the bottom panel of Fig. 7. Hardening is shown to control the range of the disorder distribution that is activated (gray dots), following the seed (red dot). When hardening is low, the damaged elements fail completely. The resulting redistribution of energy is only sufficient to trigger damage growth in the weaker elements located on the left-side of the distribution. The weaker elements are thus progressively expended and close to failure, the distribution has a leaner left-branch (curve in magenta). For the case of large hardening in regime III, the elements that are active during the cascade are stabilized immediately resulting in a rather small increase in their damage level. As a result, the elements interact with each other more frequently and reshape the whole disorder distribution (i.e., the whole damage field) as failure is approached (curve in magenta). Another consequence of large hardening

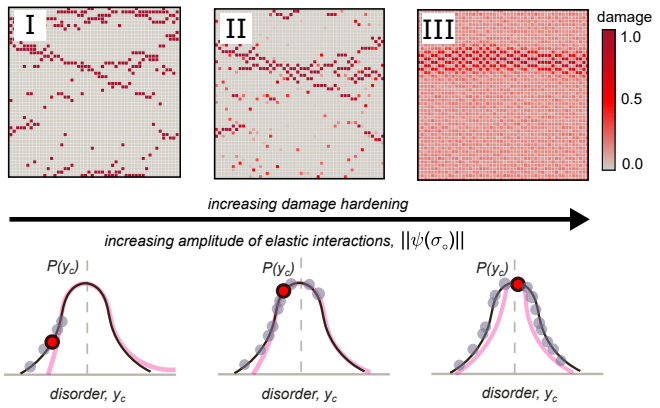

FIG. 7. Top : Typical damage field at the onset of failure for regimes I ($\eta = 0.5$), II ($\eta = 2.5$) and III ($\eta = 25$) depicting the transition from a heterogeneous to a homogeneous damage evolution. It denotes various versions of damage spreading that are dominated by material disorder and elastic interactions, respectively. Bottom: The schematic showing the activity on the distribution of disorder y_c during one damage cascade for different cases of hardening. Cascade begins with the damage evolution at the seed (red dot). We note the position of the seed for regime III could be anywhere along the distribution. The redistributions that follow may satisfy the damage criterion for other elements belonging to different regions (gray dots) of the distribution. Consequently, the original Gaussian distribution of the disorder (in black) may be transformed on approaching failure to the one shown in magenta, see also Appendix B.

is the delayed onset of failure. This allows for a larger amplitude of the elastic interactions $||\psi(\sigma_\circ)||$ as hardening is increased. Therefore, even though the elements undergo a small incremental damage, the redistributions are large. During damage evolution, even the stronger elements are activated, resulting in a rather homogeneous damage evolution.

As a result, by increasing the hardening, we shift from disorder dominated to an elastic interactions dominated damage spreading mode. At intermediate levels, damage mostly explores the weaker elements of the distribution but in contrast to regime I, the damage growth is stable. In support to this interpretation, we track the distribution $P(y_c)$ with different distances to failure and obtain a leaner left-branch in regime I and a Gaussian distribution in regime III, close to failure (see Appendix B).

D. Quasi-brittleness phase diagram

Finally, we show in Fig. 8, a 2D parametric space depicting the effect of disorder (abscissa) and hardening coefficient (ordinate). Close to the origin where disorder is weak and damage hardening is low, failure is brittle. The right-side of the diagram corresponds to the case of a rather homogeneous damage evolution (regime III). Here, the intermittent damage evolution is reminiscent of the avalanches during the depinning of a driven disordered elastic interface. The characteristic features of the precursors including their size, length scale and timescale are related to each other by scaling relations with critical exponents [40, 41]. On the left side, at moderate disorder, i.e., regime I, we expect a percolation type criticality for the precursors. Here unlike regime III, the characteristics of the cumulative damage field are described by critical exponents emerging from percolation. Following Figs. 3, 4 and 7, we also expect a cross-over, represented here as regime II where the damage spreading resembles both regimes I and III.

To obtain the bounds of the different damage spreading modes, we revisit regime I. As the elements undergo unstable damage, we seek to find the threshold value $\eta_{\rm th}$ for hardening when damage is stable. The average resistance of the damaged elements in this case, i.e., the left-branch of $P(y_c)$, is given by $Y_{\rm co} = Y_c^\circ(1 - \beta\sqrt{2/\pi})$, see Appendix C. Here $\beta\sqrt{2/\pi}$ is the mean value of the half-normal distribution describing the elements on the left branch of the disorder distribution. From the stability criterion and by considering an infinitesimal increase in damage level ($d_\circ \to 0$), we obtain

$$\eta_{\rm th} \simeq 3(1 - \beta\sqrt{2/\pi}). \tag{5}$$

The solution of the above equation is represented by the blue line in Fig. 8. It marks the upper bound for the unstable damage spreading mode (regime I). Setting $\beta = 0$ in Eq.(5) would imply disregarding the effect of disorder in the stability criterion. This is reminiscent

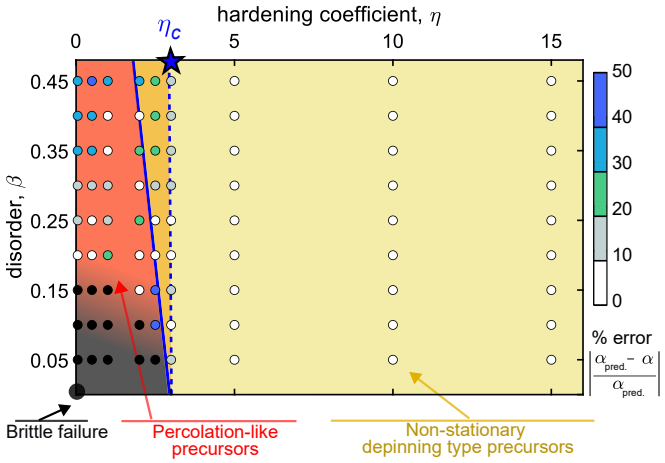

FIG. 8. Phase diagram depicting the different regimes of intermittent damage evolution during quasi-brittle failure - percolation (red) and non-stationary depinning (yellow). The narrow transition regime (orange) is bounded by the theoretical prediction Eq.(5) (blue line) and the threshold for homogeneous damage evolution (dashed line). The approach to failure in these regimes is understood to provide the scaling exponent $\alpha_{\rm pred} \simeq 0.9$ and $\alpha_{\rm pred} \simeq 0.5$, respectively. The deviation of the exponent α obtained for different values of disorder β and hardening η from the theoretical prediction is also shown (marker color).

of the damage spreading in regime III. We thus obtain $\eta_{\rm c} \simeq 3$ as the lower bound for homogeneous damage evolution (and depinning type avalanches). These predictions match rather well with the numerical results of Fig. 3. For validating the proposed scenario, the deviations $|1 - \alpha/\alpha_{\rm pred.}|$ from the predicted value $\alpha_{\rm pred.}$ are also plotted in Fig. 8 (solid circles) with $\alpha_{\rm pred.} = 0.9$ for regime I and $\alpha_{\rm pred.} = 0.5$ for regime III. We find a difference between the measured exponents and the predicted one to be less than 20%, especially at moderate disorder.

IV. DISCUSSION AND CONCLUSION

Before taking up the implications of our findings, we would like to discuss the origins of damage hardening that has been described here using a continuum mechanics approach by the hardening coefficient η. The progressive damageability at the mesoscopic scale may be attributed to both loading conditions as well as microstructural aspects. For example, during compressive failure, the activation of defects such as microcracks, porosity, etc. due to stress concentration is countered by the remotely applied stress [45–51]. As a result, on increasing the driving, the material may still resist the local loading but then displays lower stiffness. The density of microcracks therefore continues to increase until failure at which macroscopic load bearing capacity decreases owing to damage localization [1–3, 55]. On the contrary, failure under traction may result from the catastrophic growth of damage from one of the defects resulting in a relatively short damage accumulation phase. Also, the presence of confinement or temperature has been shown to influence the damage hardening behavior by altering the nature of microcracking processes : From tensile to shear cracks in crystalline rocks [62, 63], from dilatant failure to compaction shear banding in porous rocks [64] and from microcracking to plasticity in silicate rocks [65]. In porous rocks, when the intricate structure of porosity and flaws was varied, a variation in both the precursors as well as final failure is observed [66, 67]. Also, prolonged damage accumulation in complex materials is attributed to the hierarchical organization of material [23, 68, 69]. Thus, hardening can be considered as a key feature of damage evolution in brittle disordered solids. As we will discuss in the following, its influence on precursors' statistics as well as load bearing capacity have important implications for quasi-brittle failure.

The exponent α describing the divergence of precursors close to failure is an important signature of the hardening. Interestingly, this provides an explanation of the large scatter in the acoustic activity data reported in literature. To connect the acoustic emissions with damage cascades, we use the empirical relation $\alpha_{N_{\rm AE}} \simeq 1.3\,\alpha$ recently reported in the literature [41, 44]. This relation is consistent with our theoretical understanding of acoustic emissions: Damage cascades are composed of several highly correlated clusters and each of them may lead to individual acoustic hits. Therefore, the waiting times between successive damage cascades are exponentially distributed as expected for a Poissonian process whereas the waiting times between acoustic events routinely display a power law [10]. Therefore, the value of the activity rate exponent $\alpha_{N_{\rm AE}}$ is different from α. Here we can use the relation $\alpha_{N_{\rm AE}} \simeq 1.3\,\alpha$ to translate the value of α measured in our simulations to $\alpha_{N_{\rm AE}}$ that can be then compared with acoustic measurements. Close to the lower bound $\alpha_{N_{\rm AE}} \sim 0.5{-}0.8$ corresponding to $\alpha \sim 0.4{-}0.6$, we expect the damage spreading to entail large hardening. On the other hand, $\alpha_{N_{\rm AE}} \geq 1.2$ corresponding to $\alpha \geq 0.9$ points at low hardening. $\alpha_{N_{\rm AE}} \sim 1.0$, then corresponds to a transitional case where effects of both hardening and strength of disorder are at play. This interpretation also helps in rationalizing the scale-free statistics of the acoustic emissions from weakly disordered solids [17].

The smaller value of the exponent characterizing the distribution of energy of the acoustic emissions $\tau_{\rm AE}$ also may be used to qualitatively infer the hardening behavior when specimens have similar preparation methods [8, 69]. The observations of a smaller exponent for large hardening are also consistent with acoustic experiments of compressive failure of Sidorbe granite under confinement [49]. This interpretation also allows for insights on the mesoscale damage accumulation in complex materials such as bone, charcoal, etc. Smaller values of $\tau_{\rm AE}$ were reported in case of remodeled bone microstructural samples of porcine and bovine cortical bone under compression [23, 68]. The implied increase of damage hardening

is consistent with the notion that bone remodeling leads to improved properties at lower length scales. Similarly, the exponents during compressive failure of homogeneous samples of charcoal with micro- and nano-pores were reported to be smaller than the value obtained for samples with macroscopic voids and heterogeneities [70]. Nevertheless, a definitive inference of quasi-brittleness from the exponent τ_{AE} may require further study. Contrary to the scatter reported for $\alpha_{N_{\mathrm{AE}}}$, the range of the exponent τ_{AE} is narrow. Also in some materials, the mixing of signals from different sources that have different distributions may distort the inference on hardening [18, 71, 72].

The relevance of damage hardening pertains to yet another important aspect of our results - the predictability of the failure load of materials. With increasing utility of precursors in failure prediction, precise exponents based on hardening may be provided for the algorithms using numerous time-to-failure scaling laws in their monitoring systems. From an engineering perspective, it is useful to reinforce structures such that damage hardening is sufficiently large. Strategies such as confinement at the boundaries, heat treatment, etc., for example may be employed. This not only ensures the stress at failure is less sensitive to the strength of disorder at the mesoscopic scale but also facilitates an early anticipation of failure from the analysis of the larger population of precursors.

Another subtle but an important advantage of damage hardening concerns the finite-size effect. When hardening is low, the strength varies with both specimen size as well disorder [25, 31, 33]. This makes the estimation of strength in large specimens difficult as heterogeneity levels may vary with specimen size. In addition, owing to the brittle constitutive response, nucleation-type failure is anticipated at the thermodynamic limit [25, 30]. However, an enhancement to moderate hardening diminishes the influence of disorder. Failure of larger specimens is then preceded by an increased number of precursors. As a result, the effect of elastic redistributions increases manifold and the initial disorder distribution of the damage field is reshaped to a greater extent. Consequently, larger specimens may present a smaller variability of strength. A size-effect is revealed for both strength and the inter-specimen variability in this case [13, 14]. For large hardening, the damage evolution is homogeneous, even for finite-sized specimens. The size-effect on strength for this case may therefore be minimal. A detailed examination of the finite-size effects in relation to hardening is left as future studies.

In summary, we show that the damage hardening behavior of brittle disordered solids plays an integral role in the competition between disorder and elastic interactions during intermittent damage evolution until failure. It not only drives the brittle-to-ductile transition in failure behavior but also affects the statistics of the precursors. We note the linear hardening behavior considered here is rather simple. Moreover, we employ an interaction kernel derived using homogeneous damage field considerations for studying the effect of low hardening. Such considerations may not capture the finer aspects of the damage spreading in complex materials. Discrete models where interactions are implicitly defined may be better suited for the low hardening case. Still, our findings bring out the rich physics emerging from damage hardening and reconcile the existence of two universality classes of criticality discussed till date in relation to quasi-brittle failure. On one hand, the interpretation of percolation is retrieved for low hardening, similar to the discrete models such as random fuse/spring, fiber bundle, etc. On the other hand, the depinning type scaling description of precursors is disentangled from the approach of localization during compressive failure, i.e., large hardening. This conveys distinctly different interpretations for the nature of failure - a critical point and a standard instability, respectively. The signature of approaching failure is also different. The exponent is much larger for percolation. Our findings thus help unravel the connection between the level of quasi-brittleness and precursor statistics. Also, the scatter in the values of the scaling exponents reported in literature can be rationalized. These insights pave the way for quantitative inferences about quasi-brittleness of materials in real-time, a topic of strategic interest during the damage monitoring of mechanical parts and structures.

ACKNOWLEDGMENTS

We thank Laurent Ponson for the insightful discussions on the finer aspects of the damage model and their presentation. Also, we gratefully acknowledge the financial support from Sorbonne Université, CNRS and Satt-Lutech through the project, *Development of a technology of predictive maintenance for materials and structures under compression* and from the National Center for Space Studies for the project, *From diagnostic to prognostic in structural health monitoring.*

Appendix A: Individual roles of disorder and damage hardening

The macroscopic response obtained for a fixed hardening coefficient and varying disorder is shown in different panels of Fig. 9. We note the material disorder β plays an important role when damage hardening is low. Failure is shown to occur at progressively lower value of stress and a higher value of failure strain. The transformation in damage spreading is evident on increasing the hardening coefficient η (panels from left to right). For large hardening, the value of critical stress and strain are found to be independent of the strength of disorder. On the other hand, at fixed disorder, the damage hardening results in an enhanced load bearing capacity.

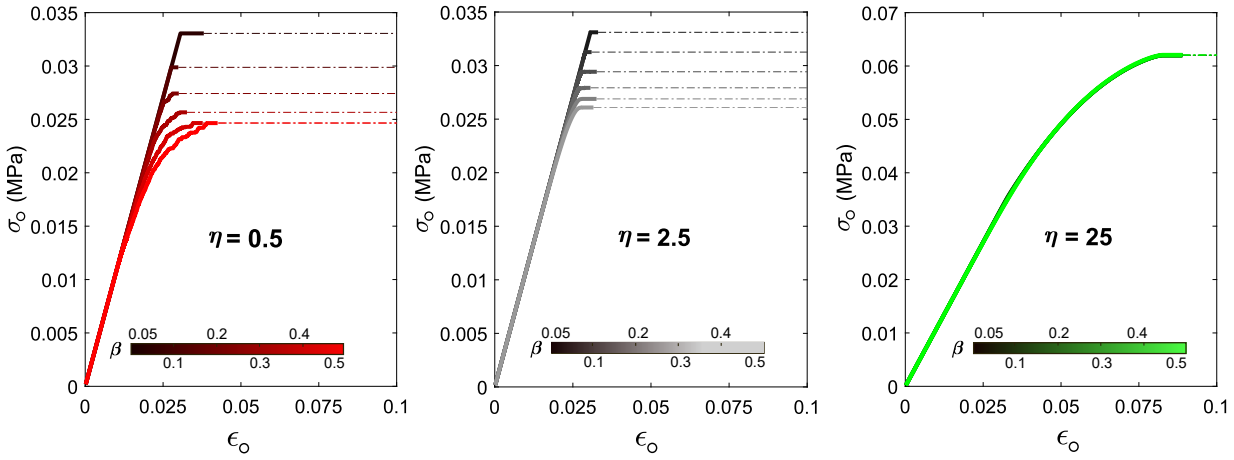

FIG. 9. The typical stress-strain response obtained for a given hardening coefficient and varying strength of disorder in each panel. Stronger disorder is shown in darker colors. The damage hardening of the data-sets increases from left to right.

Appendix B: Evolution of disorder in the damage resistance

We track the distribution of the damage resistance with distance to failure to decipher the changes in disorder with damage hardening. As shown in Fig.10 when hardening is low, the left branch of the distribution becomes progressively leaner. Only the weaker elements are expended during damage spreading. As the incremental damage in this case is large, see Fig. 5(b), the changes to the local damage resistance is very large. Consequently, these elements appear distinctly on the right branch of the distribution. Similar features are observed when the hardening is moderate. However, the partial damage of the weaker elements results in a nominal increase of the damage resistance and therefore, a second peak on the right branch is absent. We also note that the original right branch is recovered in both cases implying that the strong elements of the distribution did not participate in the damage spreading. In contrast for large hardening, the distribution becomes leaner approaching the Gaussian $\mathcal{N}(Y_{\rm co}, 0.05)$ from the original disordered field, $\mathcal{N}(Y_{\rm co}, 0.2)$. The narrow distribution close to failure rather corresponds to the hardening $Y_{\rm c}^{\circ}\eta.\delta d_{\circ}$ being drawn from a narrow Gaussian distribution with standard deviation of 0.05.

Appendix C: Threshold value of hardening for stable damage evolution

As the strength and manner of damage spreading vary with damage hardening, we expect a threshold value for hardening $\eta_{\rm th}$ at which the elastic interactions prevail over material disorder during intermittent damage evolution. Taking inspiration from the panels on the right-side in Figs. 9 and 10, we first consider the case of homogeneous damage evolution. The stability of the damage evolution given by Berthier *et al.* [54] writes as

$$\mathcal{K} = \frac{\partial(Y_{\rm co} - Y_{\circ})}{\partial d_{\circ}} \geq 0, \tag{C1}$$

where we have also considered the limiting case of the stability criterion $\mathcal{K} = 0$. Here, $Y_{\rm co}(d_{\circ})$ and $Y_{\circ}(d_{\circ})$ are the average values taken to represent the damage resistance and the damage driving force during the homogeneous damage evolution, respectively. Here $\frac{\partial Y_{\rm co}}{\partial d_{\circ}} = Y_{\rm c}^{\circ}\eta$. The average damage driving force is given by

$$Y_{\circ}(d_{\circ}) = \frac{d}{dd_{\circ}}\left(\frac{(1-\nu^2)\sigma_{\rm ext}{}^2}{2E_{\circ}}\right). \tag{C2}$$

The second term of Eq. (C1) is then given by

$$\frac{\partial Y_{\circ}}{\partial d_{\circ}} = \frac{(1-\nu^2)\sigma_{\rm ext}^2}{2}\frac{d}{dd_{\circ}}\left(\frac{-E_{\circ}'}{E_{\circ}^2}\right) \rightarrow \frac{3(1-\nu^2)\sigma_{\rm ext}^2}{E^{\circ}(1-d_{\circ})^4}, \tag{C3}$$

where $E_{\circ}(d_{\circ}) = E^{\circ}(1-d_{\circ})^2$ and $E_{\circ}'(d_{\circ}) = -2E^{\circ}(1-d_{\circ})$. From the equilibrium condition $Y_{\circ}(d_{\circ}) = Y_{\rm co}(d_{\circ})$, we have $\sigma_{\rm ext}^2 = \frac{Y_{\rm co}E^{\circ}(1-d_{\circ})^3}{(1-\nu^2)}$. We thus obtain the second term of Eq. (C1) as

$$\frac{\partial Y_{\circ}}{\partial d_{\circ}} = \frac{3Y_{\rm c}^{\circ}(1+\eta d_{\circ})}{(1-d_{\circ})}. \tag{C4}$$

The terms of the stability criterion given in Eq.(C1) can be then rearranged as

$$\eta \geq \frac{3(1+\eta d_{\circ})}{(1-d_{\circ})}. \tag{C5}$$

For the incremental damage to be stable, we take $d_{\circ} \rightarrow \delta d_{\circ} \sim 0$ and obtain the threshold value $\eta_{\rm c} \simeq 3$ for stable homogeneous damage evolution. When $\eta < \eta_{\rm c}$, the damage spreading is dominated by the strength of the material disorder β. Close to $\eta_{\rm c}$, one then expects a transition where the incremental damage of the elements is

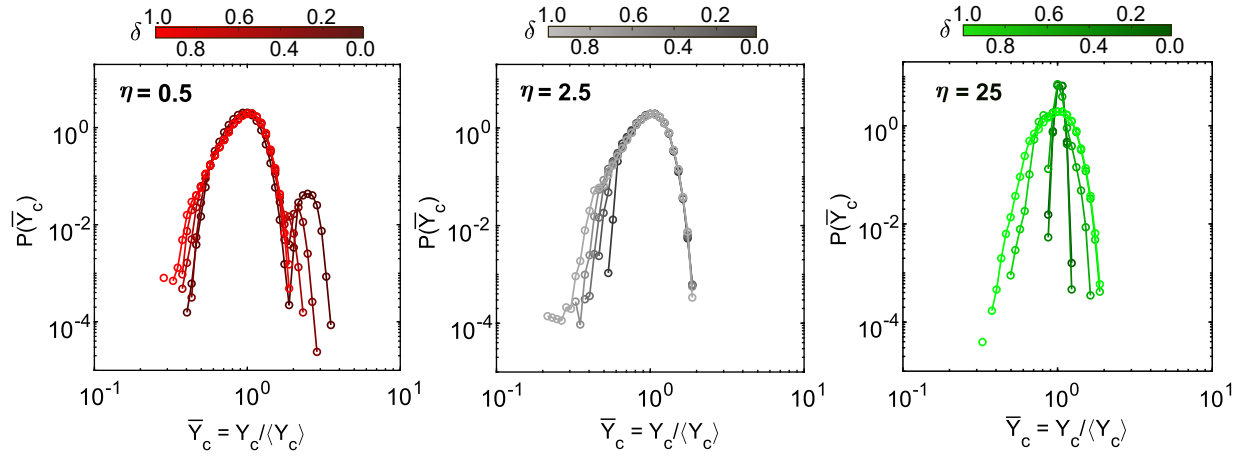

FIG. 10. Distribution of the damage resistance normalized by the mean value $\overline{Y_c} = Y_c/\langle Y_c\rangle$ at fixed damage hardening at different distances to failure δ. The damage hardening of the data increases from left to right.

stable. The equilibrium in this case is satisfied by the energy balance of the weaker elements whose average value $Y_\circ(d_\circ) = Y_{c\circ}(1-\beta\sqrt{2/\pi})$. Here, following Figs. 7 and 10, we consider only the left-branch of the original normal distribution. Therefore, for $\eta < \eta_c$ when disorder and elastic interactions are at play, Eq. (C4) writes as

$$\frac{\partial Y_\circ}{\partial d_\circ} = \frac{3Y_c^\circ(1+\eta d_\circ)}{(1-d_\circ)}(1-\beta\sqrt{2/\pi}). \tag{C6}$$

The hardening coefficient η to ensure stable damage growth then writes as

$$\eta \geq \frac{3(1-\beta\sqrt{2/\pi})}{1-d_\circ[1+3(1-\beta\sqrt{2/\pi})]}. \tag{C7}$$

Again by considering $d_\circ \to \delta d_\circ \simeq 0$, we obtain the threshold value $\eta_{\rm th}$ of damage hardening as

$$\eta_{\rm th} \simeq 3(1-\beta\sqrt{2/\pi}). \tag{C8}$$

[1] M. Kachanov, Elastic solids with many cracks: a simple method of analysis, International Journal of Solids and Structures **23**, 23 (1987).

[2] Z. P. Bažant, Nonlocal damage theory based on micromechanics of crack interactions, Journal of engineering mechanics **120**, 593 (1994).

[3] M. J. Alava, P. K. Nukala, and S. Zapperi, Statistical models of fracture, Advances in Physics **55**, 349 (2006).

[4] D. Lockner, J. Byerlee, V. Kuksenko, A. Ponomarev, and A. Sidorin, Quasi-static fault growth and shear fracture energy in granite, Nature **350**, 39 (1991).

[5] J. Fortin, S. Stanchits, G. Dresen, and Y. Guéguen, Acoustic emission and velocities associated with the formation of compaction bands in sandstone, Journal of Geophysical Research: Solid Earth **111** (2006).

[6] A. Petri, G. Paparo, A. Vespignani, A. Alippi, and M. Costantini, Experimental evidence for critical dynamics in microfracturing processes, Physical Review Letters **73**, 3423 (1994).

[7] A. Garcimartin, A. Guarino, L. Bellon, and S. Ciliberto, Statistical properties of fracture precursors, Physical Review Letters **79**, 3202 (1997).

[8] S. Deschanel, L. Vanel, N. Godin, G. Vigier, and S. Ciliberto, Experimental study of crackling noise: conditions on power law scaling correlated with fracture precursors, Journal of Statistical Mechanics: Theory and Experiment **2009**, P01018 (2009).

[9] J. Davidsen, S. Stanchits, and G. Dresen, Scaling and universality in rock fracture, Physical review letters **98**, 125502 (2007).

[10] J. Baró, Á. Corral, X. Illa, A. Planes, E. K. Salje, W. Schranz, D. E. Soto-Parra, and E. Vives, Statistical similarity between the compression of a porous material and earthquakes, Physical review letters **110**, 088702 (2013).

[11] J. Rosti, J. Koivisto, and M. J. Alava, Statistics of acoustic emission in paper fracture: precursors and criticality, Journal of Statistical Mechanics: Theory and Experiment **2010**, P02016 (2010).

[12] L. Girard, D. Amitrano, and J. Weiss, Failure as a critical phenomenon in a progressive damage model, Journal of Statistical Mechanics: Theory and Experiment **2010**, P01013 (2010).

[13] J. Weiss, L. Girard, F. Gimbert, D. Amitrano, and D. Vandembroucq, (finite) statistical size effects on compressive strength, Proceedings of the National Academy of Sciences **111**, 6231 (2014).

[14] C.-C. Vu, D. Amitrano, O. Plé, and J. Weiss, Compressive failure as a critical transition: Experimental evidence and mapping onto the universality class of depinning, Phys. Rev. Lett. **122**, 015502 (2019).

[15] J. Baró, K. A. Dahmen, J. Davidsen, A. Planes, P. O. Castillo, G. F. Nataf, E. K. Salje, and E. Vives, Experimental evidence of accelerated seismic release with-

out critical failure in acoustic emissions of compressed nanoporous materials, Physical review letters **120**, 245501 (2018).
[16] J. Baró, A. Planes, E. K. Salje, and E. Vives, Fracking and labquakes, Philosophical Magazine **96**, 3686 (2016).
[17] G. F. Nataf, P. O. Castillo-Villa, J. Baró, X. Illa, E. Vives, A. Planes, and E. K. Salje, Avalanches in compressed porous Si O2-based materials, Physical Review E **90**, 022405 (2014).
[18] J. Davidsen, T. Goebel, G. Kwiatek, S. Stanchits, J. Baró, and G. Dresen, What controls the presence and characteristics of aftershocks in rock fracture in the lab?, Journal of Geophysical Research: Solid Earth **126**, e2021JB022539 (2021).
[19] L. Wang, S. Cao, X. Jiang, and E. K. Salje, Cracking of human teeth: An avalanche and acoustic emission study, Journal of the Mechanical Behavior of Biomedical Materials **122**, 104666 (2021).
[20] S.-T. Tsai, L.-M. Wang, P. Huang, Z. Yang, C.-D. Chang, and T.-M. Hong, Acoustic emission from breaking a bamboo chopstick, Physical Review Letters **116**, 035501 (2016).
[21] D. Triantis and S. K. Kourkoulis, An alternative approach for representing the data provided by the acoustic emission technique, Rock Mechanics and Rock Engineering **51**, 2433 (2018).
[22] We consider Omori law, the scaling relation associated with the activity rate of events between two successive large signals to also describe the approach to failure [10].
[23] J. Baró, P. Shyu, S. Pang, I. M. Jasiuk, E. Vives, E. K. Salje, and A. Planes, Avalanche criticality during compression of porcine cortical bone of different ages, Physical Review E **93**, 053001 (2016).
[24] S. Roux, A. Hansen, H. Herrmann, and E. Guyon, Rupture of heterogeneous media in the limit of infinite disorder, Journal of statistical physics **52**, 237 (1988).
[25] A. Hansen, E. L. Hinrichsen, and S. Roux, Scale-invariant disorder in fracture and related breakdown phenomena, Physical Review B **43**, 665 (1991).
[26] D. Sornette, Sweeping of an instability: an alternative to self-organized criticality to get power laws without parameter tuning, J. Phys. I **4**, 209 (1994).
[27] S. Zapperi, P. Ray, H. E. Stanley, and A. Vespignani, First-order transition in the breakdown of disordered media, Physical review letters **78**, 1408 (1997).
[28] S. Zapperi, P. Ray, H. E. Stanley, and A. Vespignani, Avalanches in breakdown and fracture processes, Physical Review E **59**, 5049 (1999).
[29] Y. Moreno, J. Gomez, and A. Pacheco, Fracture and second-order phase transitions, Physical review letters **85**, 2865 (2000).
[30] A. Shekhawat, S. Zapperi, and J. P. Sethna, From damage percolation to crack nucleation through finite size criticality, Physical review letters **110**, 185505 (2013).
[31] S. Biswas, S. Roy, and P. Ray, Nucleation versus percolation: Scaling criterion for failure in disordered solids, Physical Review E **91**, 050105 (2015).
[32] H. B. da Rocha and L. Truskinovsky, Rigidity-controlled crossover: From spinodal to critical failure, Physical Review Letters **124**, 015501 (2020).
[33] V. Kádár, Z. Danku, and F. Kun, Size scaling of failure strength with fat-tailed disorder in a fiber bundle model, Physical Review E **96**, 033001 (2017).
[34] S. Roy, S. Biswas, and P. Ray, Modes of failure in disordered solids, Physical Review E **96**, 063003 (2017).
[35] D. Kumar, A. Banerjee, and R. Rajesh, Interplay between disorder and hardening during tensile fracture of a quasi-brittle solid, Proceedings of the Royal Society A **478**, 20210934 (2022).
[36] C. D. Ferguson, W. Klein, and J. B. Rundle, Spinodals, scaling, and ergodicity in a threshold model with long-range stress transfer, Physical Review E **60**, 1359 (1999).
[37] O. E. Yewande, Y. Moreno, F. Kun, R. C. Hidalgo, and H. J. Herrmann, Time evolution of damage under variable ranges of load transfer, Physical Review E **68**, 026116 (2003).
[38] J. T. Kjellstadli, E. Bering, M. Hendrick, S. Pradhan, and A. Hansen, Can local stress enhancement induce stability in fracture processes? part i: Apparent stability, Frontiers in Physics **7**, 105 (2019).
[39] S. Sinha, S. Roy, and A. Hansen, Crack localization and the interplay between stress enhancement and thermal noise, Physica A: Statistical Mechanics and its Applications **569**, 125782 (2021).
[40] E. Berthier, A. Mayya, and L. Ponson, Damage spreading in quasi-brittle disordered solids: Ii. what the statistics of precursors teach us about compressive failure, Journal of the Mechanics and Physics of Solids **162**, 104826 (2022).
[41] A. Mayya, E. Berthier, and L. Ponson, How criticality meets bifurcation in compressive failure of disordered solids, Physical Review X (accepted, in production); arXiv:2207.12270 (2023).
[42] O. Narayan and D. S. Fisher, Threshold critical dynamics of driven interfaces in random media, Physical Review B **48**, 7030 (1993).
[43] K. J. Wiese, Theory and experiments for disordered elastic manifolds, depinning, avalanches, and sandpiles, Reports on Progress in Physics **85**, 086502 (2022).
[44] A. Mayya, E. Berthier, and L. Ponson, Procédé et dispositif d'analyse d'une structure. french patent application fr2002824 (2020).
[45] M. Kiyoo, Pressure dependence of rock strength and transition from brittle fracture to ductile flow, Bulletin of the Earthquake Research Institute **44**, 215 (1966).
[46] B. Evans, J. T. Fredrich, and T.-F. Wong, The brittle-ductile transition in rocks: Recent experimental and theoretical progress, The brittle-ductile transition in rocks **56**, 1 (1990).
[47] D. Amitrano, J.-R. Grasso, and D. Hantz, From diffuse to localised damage through elastic interaction, Geophysical research letters **26**, 2109 (1999).
[48] C. E. Renshaw and E. M. Schulson, Universal behaviour in compressive failure of brittle materials, Nature **412**, 897 (2001).
[49] D. Amitrano, Brittle-ductile transition and associated seismicity: Experimental and numerical studies and relationship with the b value, Journal of Geophysical Research: Solid Earth **108** (2003).
[50] J. Xue, S. Hao, J. Wang, F. Ke, C. Lu, and Y. Bai, The changeable power law singularity and its application to prediction of catastrophic rupture in uniaxial compressive tests of geomedia, Journal of Geophysical Research: Solid Earth **123**, 2645 (2018).
[51] A. Cartwright-Taylor, I. G. Main, I. B. Butler, F. Fusseis, M. Flynn, and A. King, Catastrophic failure: How and when? insights from 4-d in situ x-ray microtomography, Journal of Geophysical Research: Solid Earth **125**, e2020JB019642 (2020).

[52] L. Girard, D. Amitrano, and J. Weiss, Failure as a critical phenomenon in a progressive damage model, Journal of Statistical Mechanics: Theory and Experiment **2010**, P01013 (2010).

[53] V. Dansereau, V. Démery, E. Berthier, J. Weiss, and L. Ponson, Collective damage growth controls fault orientation in quasibrittle compressive failure, Physical review letters **122**, 085501 (2019).

[54] E. Berthier, V. Démery, and L. Ponson, Damage spreading in quasi-brittle disordered solids: I. localization and failure, Journal of the Mechanics and Physics of Solids **102**, 101 (2017).

[55] J. Lemaitre, *A course on damage mechanics*, Amsterdam (Springer Verlag, 1992).

[56] S. Pradhan, A. Hansen, and P. Ray, A renormalization group procedure for fiber bundle models, Frontiers in Physics **6**, 65 (2018).

[57] A. Delaplace, G. Pijaudier-Cabot, and S. Roux, Progressive damage in discrete models and consequences on continuum modelling, Journal of the Mechanics and Physics of Solids **44**, 99 (1996).

[58] R. Ince, A. Arslan, and B. Karihaloo, Lattice modelling of size effect in concrete strength, Engineering Fracture Mechanics **70**, 2307 (2003).

[59] G.-F. Zhao, J. Fang, and J. Zhao, A 3d distinct lattice spring model for elasticity and dynamic failure, International Journal for Numerical and Analytical Methods in Geomechanics **35**, 859 (2011).

[60] G. Pijaudier-Cabot and D. Grégoire, A review of non local continuum damage: Modelling of failure?, Networks & Heterogeneous Media **9**, 575 (2014).

[61] R. C. Hidalgo, Y. Moreno, F. Kun, and H. J. Herrmann, Fracture model with variable range of interaction, Physical review E **65**, 046148 (2002).

[62] J. Escartín, G. Hirth, and B. Evans, Nondilatant brittle deformation of serpentinites: Implications for mohr-coulomb theory and the strength of faults, Journal of Geophysical Research: Solid Earth **102**, 2897 (1997).

[63] O. Katz and Z. Reches, Microfracturing, damage, and failure of brittle granites, Journal of Geophysical Research: Solid Earth **109** (2004).

[64] T.-f. Wong and P. Baud, The brittle-ductile transition in porous rock: A review, Journal of Structural Geology **44**, 25 (2012).

[65] G. Hirth and J. Tullis, The brittle-plastic transition in experimentally deformed quartz aggregates, Journal of Geophysical Research: Solid Earth **99**, 11731 (1994).

[66] J. Vasseur, F. B. Wadsworth, M. J. Heap, I. G. Main, Y. Lavallée, and D. B. Dingwell, Does an inter-flaw length control the accuracy of rupture forecasting in geological materials?, Earth and Planetary Science Letters **475**, 181 (2017).

[67] J. Ritter, S. Shegufta, and M. Zaiser, Effects of disorder on deformation and failure of brittle porous materials, Journal of Statistical Mechanics: Theory and Experiment **2023**, 053301 (2023).

[68] A. Mayya, A. Banerjee, and R. Rajesh, Role of porosity and matrix behavior on compressive fracture of haversian bone using random spring network model, Journal of the Mechanical Behavior of Biomedical Materials **83**, 108 (2018).

[69] M. Pournajar, T. Mäkinen, S. A. Hosseini, P. Moretti, M. Alava, and M. Zaiser, Failure precursors and failure mechanisms in hierarchically patterned paper sheets in tensile and creep loading, arXiv preprint arXiv:2303.09214 (2023).

[70] Y. Xu, A. G. Borrego, A. Planes, X. Ding, and E. Vives, Criticality in failure under compression: Acoustic emission study of coal and charcoal with different microstructures, Physical Review E **99**, 033001 (2019).

[71] E. K. Salje, H. Liu, Y. Xiao, L. Jin, A. Planes, E. Vives, K. Xie, and X. Jiang, Avalanche mixing and the simultaneous collapse of two media under uniaxial stress, Physical Review E **99**, 023002 (2019).

[72] S. Senapati, A. Banerjee, and R. Rajesh, Role of composition in fracture behavior of two-phase solids, Physical Review E **107**, 055002 (2023).